Graphical Abstract

Assessing the performances of the Rain Mask Algorithm Using Long-Term NASA MPLNET Lidar Network Observations for Global Precipitation Monitoring in Preparation for the EarthCare Mission.

Simone Lolli, Jasper R. Lewis, Ali Tokay, Gemine Vivone, James R. Campbell, Erica K. Dolinar, Michael Sïcard, Adolfo Comerón, Alejandro Rodriguez-Gomez, Constantino Muñoz-Porcar, Albert García-Benadí, Mireia Udina, Joan Bech, Ellsworth J. Welton

Highlights

Assessing the performances of the Rain Mask Algorithm Using Long-Term NASA MPLNET Lidar Network Observations for Global Precipitation Monitoring in Preparation for the EarthCare Mission.

Simone Lolli, Jasper R. Lewis, Ali Tokay, Gemine Vivone, James R. Campbell, Erica K. Dolinar, Michael Sïcard, Adolfo Comerón, Alejandro Rodriguez-Gomez, Constantino Muñoz-Porcar, Albert García-Benadí, Mireia Udina, Joan Bech, Ellsworth J. Welton

- RMA demonstrates strong capabilities in detecting precipitation, including virga, achieving an accuracy of up to 72% when validated against co-located disdrometers, and surpassing IMERG in sensitivity.
- RMA was validated using data from two distinct locations (GSFC in the United States and UPC in Barcelona, Spain), showing consistent performance in identifying different precipitation events.
- RMA outperforms IMERG in sensitivity and balanced performance metrics (e.g., F1-score, Matthews Correlation Coefficient), while IMERG excels in specificity and precision, making each suitable for different scenarios.
- RMA is a valuable tool for validating ESA-JAXA's EarthCARE mission data, specifically for the Cloud Profiling Radar, enhancing global precipitation monitoring capabilities.

Assessing the performances of the Rain Mask Algorithm Using Long-Term NASA MPLNET Lidar Network Observations for Global Precipitation Monitoring in Preparation for the EarthCare Mission.

Simone Lolli[a], Jasper R. Lewis[b,c], Ali Tokay[b,c], Gemine Vivone[a], James R. Campbell[d], Erica K. Dolinar[d], Michael Sïcard[f,g], Adolfo Comerón[f], Alejandro Rodriguez-Gomez[f], Constantino Muñoz-Porcar[f], Albert García-Benadí[h], Mireia Udina[e], Joan Bech[e], Ellsworth J. Welton[b]

[a]*CNR-IMAA, Contrada S. Loja snc, Tito Scalo (PZ), 85050, Italy*
[b] Univ. of Maryland Baltimore County, NASA/GSFC, *Code 612, Greenbelt, 20771, MD, USA*
[c]*GESTAR II, Code 612, Greenbelt, 20771, MD, USA*
[d]*Naval Research Laboratory , 7 Grace Hopper Ave, Monterey, 93943, CA, USA*
[e]*Univ. of Barcelona, C/ Marti i Franques 1, Barcelona, 08028, Spain*
[f]*Univ. Polit. de Catalunya, Carrer de Jordi Girona, 31, Barcelona, 08034, Spain*
[g]*SARTI, Univ. Polit. de Catalunya, Vilanova i la Geltrú, 08800, Spain*
[h]*LACU, Université de La Réunion, Saint Denis, 97744, France*

Abstract

Accurate detection of precipitation on a global scale is essential for advancing our understanding of the hydrological cycle and improving climate models. This study evaluates the performance of the Rain Masking Algorithm (RMA), developed for NASA's Micropulse Lidar Network (MPLNET), in detecting rainfall events and distinguishing them from non-rain events over multiple years. The RMA's effectiveness was validated against data from co-located disdrometers at two distinct MPLNET sites: the Goddard Space Flight Center (GSFC) in the United States and Universitat Politècnica de Catalunya (UPC) in Barcelona, Spain. Comparisons were also conducted with precipitation retrievals from the Integrated Multi-Satellite Retrievals for GPM (IMERG) project. Results indicate that the RMA is highly effective at detecting rain events, outperforming IMERG in sensitivity and accuracy at both sites, and demonstrating also unique capability in identifying virga—precipitation that evaporates before reaching the ground (not considered in the intercomparison). However, the algorithm shows limita-

tions in identifying low-intensity precipitation and occasionally records false positives due to transient atmospheric artifacts. These findings underscore the RMA's potential for improving ground-based validation of satellite precipitation data, supporting the upcoming ESA-JAXA EarthCARE mission. This work highlights the RMA as a promising tool for refining global precipitation monitoring and advancing meteorological and climate forecasting accuracy.

Keywords: Rainfall, lidar, IMERG, Earthcare
PACS: 0000, 1111
2000 MSC: 0000, 1111

---

1. Introduction

Water is essential for all living organisms, and understanding precipitation patterns is crucial to assessing the impacts of weather and climate on the environment and society. Precipitation influences key areas such as agriculture, freshwater supplies, and the probability of natural disasters, including floods, droughts, and landslides [1, 2, 3, 4]. In many regions, precipitation serves as the primary source of drinking water and irrigation. Excess and insufficient precipitation can lead to natural disasters that severely affect communities around the world. Consequently, accurate rainfall and snowfall data are vital for planning agricultural activities, designing infrastructure, and preparing for extreme weather events. Rainfall plays an essential role in the hydrological cycle, influencing surface and groundwater resources and shaping global weather and climate patterns. To better understand precipitation and its effects, continuous and reliable global monitoring is necessary [5]. Advances in remote sensing technologies now enable scientists to gather detailed precipitation data from space, aircraft, and ground-based instruments. However, accurately detecting light precipitation events, such as virga (precipitation that evaporates before reaching the ground), remains a challenge for satellite-based methods. Although virga does not reach the surface, it plays a significant role in atmospheric water content and weather dynamics, making its detection crucial for improving weather and climate models. This gap in detecting light precipitation highlights the need for improved ground-based validation methods, particularly those that utilize lidar networks. Among these technologies, lidar has proven to be effective in detecting cloud structures, aerosols, and precipitation [6]. Ground-based

lidar can complement satellite retrieval systems by providing precise precipitation measurements across different atmospheric layers, especially in detecting phenomena such as virga that satellites often miss. However, integrating ground-based lidar data with satellite retrievals requires further validation to ensure their accuracy and applicability on a global scale.

This study focuses on validating the Rain Masking Algorithm (RMA), developed to improve lidar precipitation retrieval, and characterizing how the resulting rain occurrence frequency compares to coincident satellite retrievals. Using long-term data from the NASA MPLNET lidar network, we evaluated the performance of the RMA at two geographically distinct locations: the Goddard Space Flight Center (GSFC) and the Universitat Politècnica de Catalunya (UPC). The RMA retrievals from MPLNET and satellite retrievals from the NASA Integrated Multi-Satellite Retrievals for GPM (IMERG) project are compared rain detection from co-located in-situ PARSIVEL disdrometers. The results provide a preliminary look at how ground-based lidar rain retrievals can be used to validate liquid cloud retrieval products from the Earth Clouds, Aerosols and Radiation Explorer (EarthCARE) mission, as described by [7]. EarthCARE, a collaboration between the European Space Agency (ESA) and the Japan Aerospace Exploration Agency (JAXA), aims to enhance global understanding of cloud-aerosol interactions and their impact on Earth's radiation budget [8, 9]. This intercomparison provides a comprehensive evaluation of the effectiveness of RMA, supporting its role in validating EarthCARE's Cloud Profiling Radar (CPR), launched in May 2024. The 94 GHz CPR is the first spaceborne Doppler radar and is expected to provide improved rain detection compared to CloudSat [10].

The research emphasizes the importance of accurately validating precipitation retrieval algorithms, particularly the RMA, to enhance the precision of satellite-derived measurements. It tackles the challenge of detecting light precipitation, such as virga, often missed by satellite observations. This validation, using ground-based lidar data and comparing with IMERG, aims to improve global precipitation estimates and refine weather and climate forecasts, thus advancing global precipitation monitoring systems.

2. Methods and Materials

2.1. Instruments

Disdrometer

The Parsivel disdrometer is a widely used instrument to measure the raindrop size distribution and rainfall intensity. This sophisticated device provides high-resolution data, which makes it essential in meteorology and hydrology [11]. Its ability to capture the microphysical aspects of precipitation events is crucial to evaluate satellite-based rainfall products, particularly to validate the Integrated Multi-Satellite Retrievals for GPS (IMERG) algorithm [12]. By comparing the intensity of the rain on the disdrometer with the IMERG estimates, we assess the precision and reliability of the satellite-based precipitation measurement methodology [13]. This comparison helps refine meteorological, hydrological, and climate models, improving our understanding of the limitations and strengths of satellite precipitation products.

The Parsivel disdrometer uses advanced laser technology to determine the size and velocity of the raindrops. Unlike traditional rain gauges, it offers comprehensive insight into precipitation events by capturing the entire raindrop size range using laser optics. This real-time data improves weather prediction, flood forecasting, and water resource management [14, 15]. The data in this study has a 60 second temporal resolution and provide information on rainfall intensity, droplet size distribution, and other microphysical characteristics. The disdrometer can detect raindrops ranging from 0.2 to 25 mm in diameter, allowing it to capture a variety of precipitation types, including rain, snow, sleet and hail. For Barcelona site, the Parsivel disdrometer is about 600 m from the MPLNET lidar, at the Faculty of Physics building of the University of Barcelona as described in [16].

Network of lidar instruments: NASA MPLNET

Lidar, which stands for Light Detection and Ranging, is a prominent active remote sensing technology that originated in the 1960s of the 20th century. Its adoption and widespread popularity increased following the development of the CO_2 laser[17]. Provides high-resolution vertical profiles of aerosols, clouds, and gases, providing key insights into their optical and microphysical characteristics. Lidar has been instrumental in studies that involve monitoring air quality [18], analysis of cloud structure [19, 20, 21], and tracking of atmospheric gases such as carbon dioxide [22] and methane [23]. The spatial and temporal precision of lidar observations makes it ideal for studying atmospheric dynamics at both local and regional scales.

NASA's Micropulse Lidar Network (MPLNET) represents a global lidar

system designed for continuous monitoring of atmospheric properties. Established in 1999, MPLNET uses elastic MPL systems, originally developed by SigmaSpace, as part of NASA's Earth Observing System (EOS) program[24]. The network instruments take measurements every minute, extending from the surface up to 30 km, with vertical resolutions of 30 m and 75 m. This global coverage, with stations deployed in the polar, mid-latitude, tropical, and equatorial regions, captures critical data on the optical properties of aerosols and clouds [25], contributing to a better understanding of atmospheric processes and their radiative impacts.

MPLNET data products [26] follow the AERONET-derived EOS format, including the Level 1 (L1), Level 1.5 (L15) and Level 2 (L2) data. L1 and L15 data are freely available in near-real time, while L2 products are available upon request. In 2017, MPLNET added a polarized channel [27], providing more detailed information on particle morphology, particularly for precipitation detection. The Goddard Space Flight Center (GSFC) and Universitat Politècnica de Catalunya (UPC) stations, key contributors to this study, demonstrate the ability of MPLNET to enhance atmospheric dynamics research through long-term lidar observations.

Satellite retrievals: the IMERG product

The Integrated Multi-Satellite Retrievals for GPM (IMERG; [28]) product is a satellite-based precipitation data set that provides global rainfall estimates. IMERG integrates data from various satellite sensors, including passive microwave and infrared imagers, to generate high-resolution precipitation maps with both fine temporal (30 minute) and spatial (0.1 deg. X 0.1 deg.) scales. It incorporates data from the Global Precipitation Measurement (GPM; [29]) constellation, which collects crucial precipitation parameters such as cloud properties, rainfall intensity, and rainfall drop size distribution. This integration enables IMERG to overcome the limitations of individual satellite sensors and provides accurate and reliable global precipitation estimates.

IMERG is widely used in hydrological and meteorological applications, including flood forecasting, drought monitoring, and climate analysis [30, 31]. Its high temporal and spatial resolution, combined with global coverage, makes it a valuable tool for analyzing precipitation variability, studying extreme weather events, and validating numerical weather prediction models [32, 33]. This study uses IMERG Version 06, Final run, which merges data

from the Tropical Rainfall Measuring Mission (TRMM) and GPM, allowing comparisons of past and present precipitation data. This extended dataset improves the accuracy of climate models and supports applications in disaster response, resource management, and food security.

2.2. Rain Retrieval/Measurement Methods

The Rain Masking Algorithm

The Rain Masking Algorithm (RMA), shown schematically in Figure 1, processes composite images of the Volume Depolarization Ratio (VDR) derived from the MPLNET L15 Normalized Relative Backscatter (NRB) product. Each day, a composite image of the backscattered signal is generated, providing profiles with a 1 minute temporal resolution and a vertical resolution of 0.075 km, extending from the surface up to 30 km. The algorithm applies to VDR data beneath cloud bases, as precipitation is only expected below clouds [25]. The bins are classified as rain when the VDR exceeds 0.06, following the threshold established by [34]. Non-rainy bins are identified when no cloud is present or VDR falls below this threshold. To optimize this threshold, we performed a sensitivity study, testing a range of VDR values to identify the setting that maximizes detection accuracy while minimizing false positives and false negatives. During the study, we evaluated thresholds from 0.01 to 0.07 in multiple data sets from the GSFC and UPC sites, analyzing the true/false positive/negative events for each threshold. The results (not shown here) indicated that a VDR threshold of 0.06 consistently provided the best balance minimizing misclassifications of atmospheric aerosols or non-precipitation events such as rain. Lower thresholds, while improving the sensitivity slightly, resulted in higher false-positive rates. In contrast, higher thresholds led to underdetection of light precipitation events, reducing the sensitivity of the algorithm, especially in cases of low intensity rainfall. The initial classification of the RMA is refined by estimating the parameters of the Laplace distributions for both rain and non-rain scenarios, and a Maximum Posteriori (MAP) detector is applied to estimate an accurate rain mask [35]. Post-processing uses morphological operators to minimize image noise and eliminate non-physical detections. The final rain mask classifies the conditions into four categories: (1) rain that reaches the ground, (2) virga (rain that evaporates before reaching the surface), (3) no precipitation, and (4) signal attenuation due to the insufficient signal-to-noise ratio.

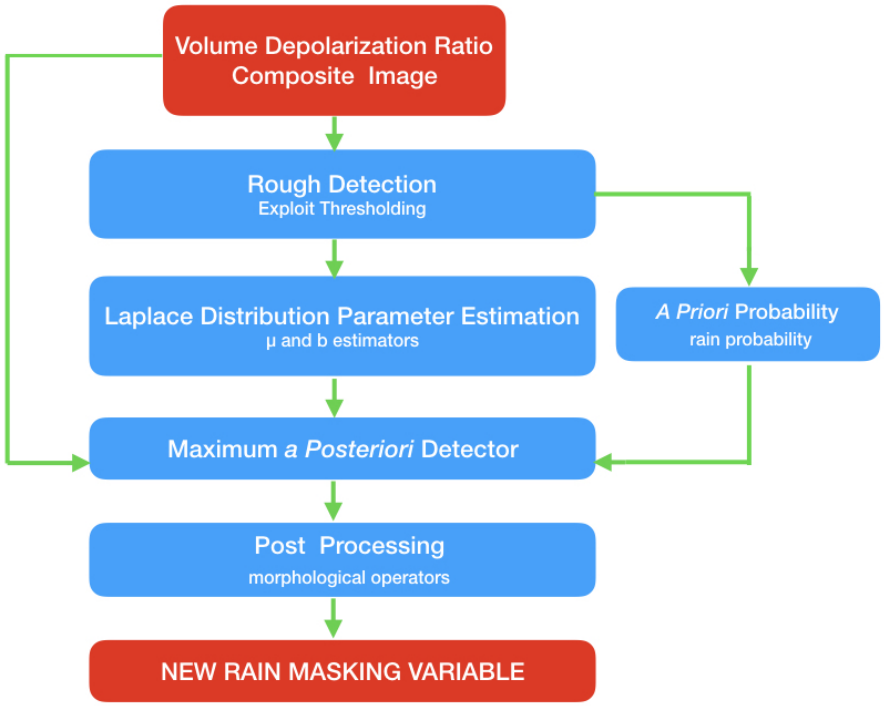

Figure 1: Flowchart of V3 MPLNET rain detection algorithm. Red boxes indicate data input/output, while blue boxes represent the processing steps.

The current configuration of the RMA (see Table 2) is optimized to detect rain events with a minimum duration of 5 minutes, for cloud bases at least 300 meters above the ground.

Parameter	**Value**
Min Cloud Base (Above Ground Level)	300 m
Min precipitation duration (over 60 min)	5 min
VDR Threshold	0.06

Table 1: Configuration of the Rain Masking Algorithm

3. Validation Protocol

To evaluate the effectiveness of the Rain Masking Algorithm (RMA), we used a binary classification of rain versus no-rain events. The microphysical properties of precipitation were not analyzed. Both the IMERG rainfall intensity (30 minute temporal resolution) and the disdrometer rainfall intensity (60 second temporal resolution) were converted into binary rain/no-rain categories. The intercomparison involved aggregating the data into 60-minute bin intervals to ensure consistency across the datasets. A bin is classified as a rain event if precipitation is detected for a minimum duration of five minutes within the 60-minute interval for both the Rain Masking Algorithm (RMA) and the disdrometer. IMERG's classification was based on any precipitation detected during the 30 min interval. Events where the lidar signal was fully attenuated or the precipitation did not reach the surface were excluded from the intercomparison.

The validation data set is made up of two complete years from the UPC, covering 2019 and 2020, along with partial data collected from GSFC, spanning the years 2020 to 2022. The availability of data for each site is summarized in Table 2.

	2019	2020	2021	2022
GSFC	—	Jan-Feb	Feb-June	Feb-May
UPC	Jan-Dec	Jan-Dec	—	—

Table 2: Data availability at each MPLNET station

To balance the dataset, where non-rain events typically outnumber rain events, we applied a random selection method to ensure equal representation. First, the number of non-rain events was determined, followed by random sampling to match the number of rain events. This balanced dataset allowed for a more accurate comparison between rain and non-rain events.

4. Results

We compare the results of the rain mask algorithm and the IMERG project with observations from a co-located disdrometer. Taking the disdrometer as a benchmark, the contingency table or confusion matrix [36] is derived (Figure 2) as well as several statistical metrics, including:

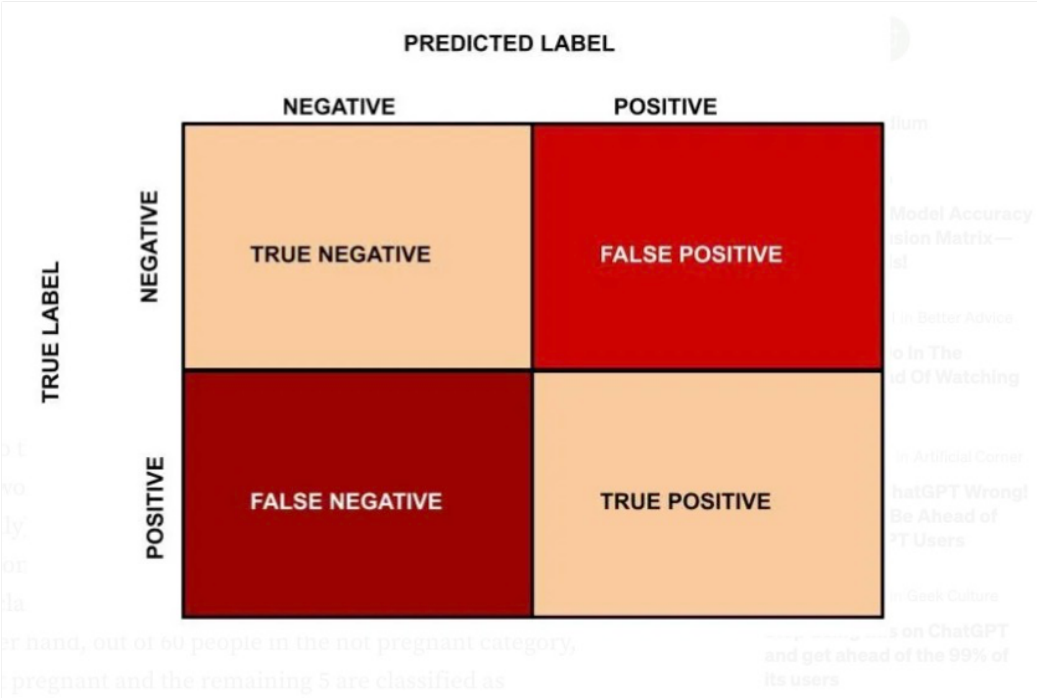

Figure 2: Confusion Matrix. Predicted label is the outcome from the rain mask algorithm or IMERG, while true label is obtained from the disdrometer

Accuracy: The accuracy reflects the general accuracy of the algorithm. Calculated by taking the ratio of correctly predicted events to the total events.

$$\frac{TN + TP}{TN + FP + TP + FN} \tag{1}$$

where TN stands for True Negative, TP stands for True Positive, while FN and FP represent false positive and negative, respectively.

Precision: Precision quantifies the proportion of correctly detected rain events by the algorithm among all rain events from the disdrometer.

$$\text{Precision} = \frac{TP}{TP + FP} \tag{2}$$

Error: The error rate is the complement of precision and represents the proportion of misclassified rain events.

$$\text{Error Rate} = 1 - \text{Precision} \tag{3}$$

Sensitivity: Sensitivity, also known as recall or true positive rate, measures the proportion of actual detected rain events correctly identified by the rain mask algorithm.

$$\text{Sensitivity} = \frac{\text{TP}}{\text{TP} + \text{FN}} \tag{4}$$

Specificity: Specificity measures the proportion of actual no-rain events correctly identified by the rain mask algorithm.

$$\text{Specificity} = \frac{TN}{TN + FP} \tag{5}$$

False Positive Rate: The false positive rate is the proportion of actual events without rain that are incorrectly classified as rain events by the rain mask algorithm.

$$\text{FPR} = \frac{FP}{FP + TN} \tag{6}$$

F1-score: The F1-score is the harmonic mean of precision and sensitivity. Provides a balanced measure of the accuracy of the rain mask algorithm considering both false positives and false negatives.

$$F_1 = 2 \cdot \frac{\text{Precision} \cdot \text{Sensitivity}}{\text{Precision} + \text{Sensitivity}} \tag{7}$$

Matthews Correlation Coefficient: The Matthews Correlation Coefficient (MCC) is a measure of the quality of binary classifications, considering all four possible outcomes (true positive, true negative, false positive, and false negative).

$$MCC = \frac{TP \cdot TN - FP \cdot FN}{\sqrt{(TP + FP)(TP + FN)(TN + FP)(TN + FN)}} \tag{8}$$

Kappa: Kappa, also known as Cohen's kappa, measures the agreement between the rain mask algorithm detection and actual classifications, considering the agreement that could be expected by chance alone.

$$\kappa = \frac{P_d - P_r m}{1 - P_r m} \tag{9}$$

where P_d and $P_r m$ are the rain episodes detected by the disdrometer and those detected by RMA/IMERG.

4.1. GSFC

Data for intercomparison were collected discontinuously at the GSFC from February 2020 to May 2022 (see Tab. 2, during which the disdrometer recorded 262 precipitation events.

Metric	RMA	IMERG
Accuracy	0.72	0.66
Error Rate	0.28	0.34
Sensitivity (Recall)	0.63	0.40
Specificity	0.81	0.91
Precision	0.78	0.83
False Positive Rate	0.19	0.09
F1 Score	0.69	0.54
MCC	0.46	0.37
Kappa	0.41	0.29

Table 3: Intercomparison of Statistical Parameters for MPL and IMERG (GSFC Dataset)

Comparison of RMA and IMERG against the disdrometer considered as reference highlights the unique characteristics of each technique. When considering accuracy, RMA achieves a higher value of 72% compared to IMERG (66%), indicating that RMA has a better overall performance in correctly predicting both positive and negative cases. However, when examining specificity, IMERG outperforms RMA with a value of 91% versus 81%. This suggests that IMERG is more effective in correctly identifying non-precipitation events, which makes it more reliable when minimizing false positives is crucial.

In contrast, sensitivity (recall), which measures the ability to correctly identify positive cases, is significantly higher for RMA at 63% compared to IMERG at 40%. This indicates that the RMA has a stronger capacity to detect true positive rain events, which could be particularly beneficial in applications where missing positive cases is more important. Additionally, the precision metric slightly favors IMERG, which achieves 83% over RMA's 78%. Higher precision for IMERG implies that, among the positive predictions it makes, a higher proportion is correct, correlated with IMERG's notably lower false Positive Rate of 9% compared to 19% for RMA.

When considering balanced performance metrics such as the F1 score, Matthews' correlation coefficient (MCC) and Kappa, RMA consistently performs better with values of 0.69, 0.46, and 0.41, respectively, compared to

IMERG's 0.54, 0.37, and 0.29. These metrics suggest that RMA maintains a more balanced trade-off between precision and recall and is overall in better agreement with the ground truth.

RMA is preferable in scenarios where it is essential to maximize sensitivity and maintain a balanced performance between precision and recall, as indicated by its higher F1 score, MCC, and Kappa. However, IMERG is more suitable for situations where high specificity and precision are prioritized, as it effectively minimizes false positives and achieves a higher true negative rate.

In Table 4 we report the confusion matrix for Disdrometer - RMA for the cases under investigation. As noted previously, no-rain events are randomly selected to match the same number of precipitation events. RMA shows better performance than IMERG (Table 5)

		RMA		
		No Rain	Rain	Total
Disdrometer	No Rain	215(82%)	48(18%)	263
	Rain	97(37%)	165(63%)	262
	Total	312	213	525

Table 4: Confusion Matrix Disdrometer - Rain Masking Algorithm

In Table 4, the RMA accurately identified 215 instances of 'no rain', representing 82% of all such cases. However, there were 48 instances where the RMA indicated 'rain' that was undetected by the disdrometer, resulting in a 18% error rate. Furthermore, the RMA failed to detect 97 rain events, classifying them as 'no rain', which corresponds to an error rate of 37%. On a positive note, the RMA correctly identified 165 'Rain' events, accounting for 63% of the total 'Rain' events recorded by the disdrometer.

In Table 5, IMERG accurately detected 241 no-rain events, representing 91% of such cases, but missed 157 rain events, which account for 60% of the instances. As mentioned earlier, IMERG is less likely to generate false positives but tends to have more false negatives compared to RMA.

		IMERG		
		No Rain	Rain	Total
Disdrometer	No Rain	241(91%)	22(9%)	263
	Rain	157(60%)	105(40%)	262
	Total	398	127	525

Table 5: Confusion Matrix Disdrometer - IMERG. Satellite retrievals fail to capture more than half of all precipitation events.

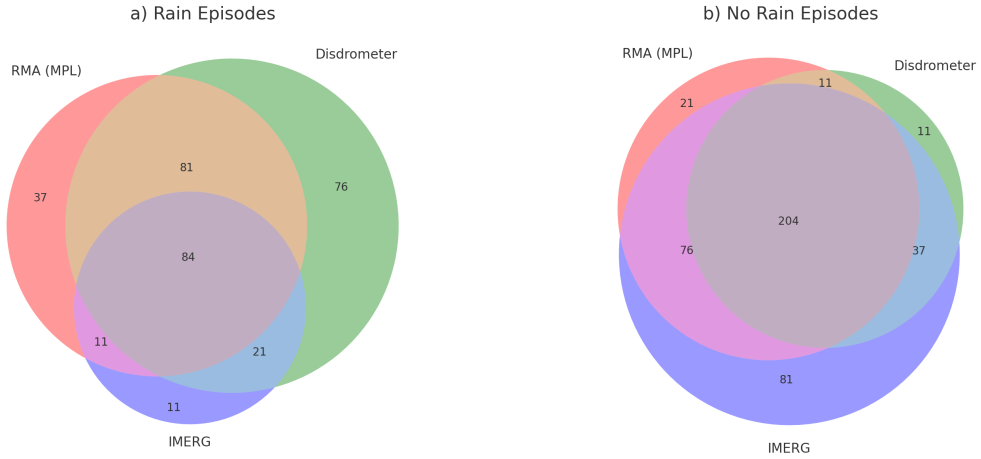

Figure 3: Venn diagrams showing the overlap in detection of rain and no-rain events among IMERG, RMA, and the Disdrometer at GSFC. The numbers indicate the detected cases shared between the instruments as well as those unique to each, highlighting the performance of IMERG and RMA compared to the disdrometer.

To provide a comprehensive understanding, we examine the Venn diagram in Figure 3, which shows the detection of individual rainfall events by RMA and IMERG compared to the total of 525 events, with 262 rain events identified by the disdrometer considered the reference. RMA has 37 unique precipitation events that were not recorded by the disdrometer (false positives) or IMERG , while the disdrometer recorded 76 precipitation events undetected by RMA and IMERG. This represents data specific to the disdrometer's sensitivity or conditions it was able to detect that the others did not. However, IMERG has only 11 false positives. Regarding intersections, there are 81 common rain events that the RMA and the disdrometer detected, indicating a moderate level of agreement, while the overlap restricted solely to IMERG and the disdrometer is 21 rainfall events, which is lower than

the overlap for the RMA. The three instruments detected 84 rain events. This central overlap indicates strong consistency for these cases, suggesting that when all three instruments detect an event, it is highly reliable. The distribution of unique and overlapping observations helps us to understand the differences in reliability, coverage, and sensitivity among the instruments. This can guide further analysis on calibrations, data integration strategies, and identifying complementary strengths for meteorological studies.

In general, for the intercomparison at GSFC, RMA shows superior performance compared to IMERG in most evaluation metrics. Specifically, RMA exhibits improved precision, specificity, precision, and F1 score, along with reduced error rates and false positive rates. The elevated RMA Matthews Correlation Coefficient (MCC) and Kappa values further substantiate a more robust concordance and correlation with actual precipitation events. Despite both models manifesting high sensitivity in rain detection, RMA delivers a more balanced and reliable performance, particularly in the accurate identification of rainfall events and the mitigation of false positive occurrences.

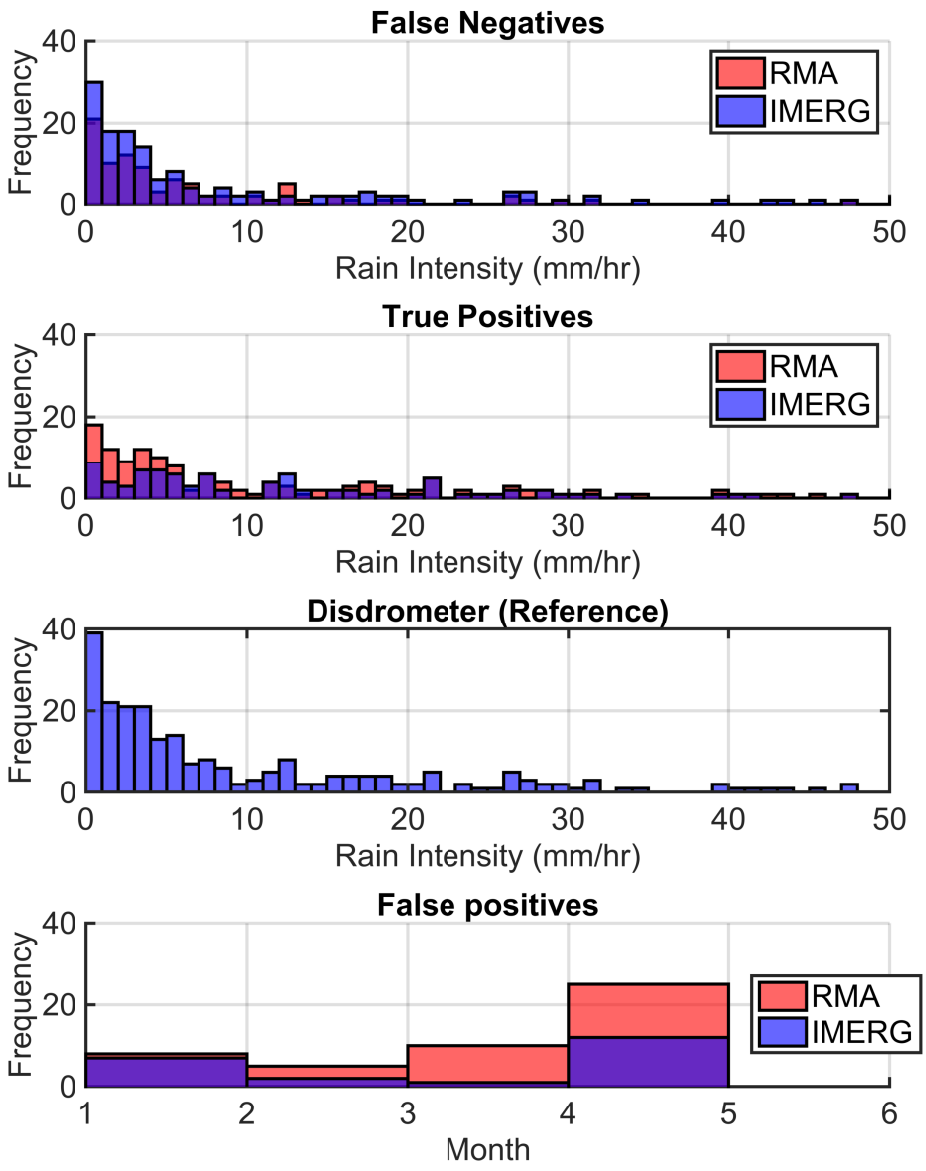

Figure 4: Above: Histogram of false negative events. Middle 1: Histogram of the true positive events detection. Middle 2: Disdrometer rain event intensities histogram Lower: Histogram of false positives with respect to month. Frequency is expressed in absolute (%) values.

Next, we analyze how the algorithms react to the varying intensities of the rain as measured by the disdrometer. Figure 4 displays histograms that illustrate the precision of RMA and IMERG rain detection. Histograms categorize results into undetected rain (false negatives), true positives, and false positives, based on the intensity of the rain recorded by the disdrometer. False positives are analyzed vs. month. IMERG (in blue) has a significantly higher frequency of undetected rain, especially at lower rain intensities (0-5 mm/hr). This suggests that IMERG is missing more rain events than RMA (in red) in the low-intensity range. At higher rain intensities, both systems exhibit very few undetected rain events, although IMERG shows slightly more missed detections. When it comes to correctly identified precipitation events, RMA outperforms IMERG for intensities between 0.5 and 6 mm/hr; however, for higher rainfall rates, their performance is nearly identical, even if those events are scarce in number. Concerning false positives, the RMA reaches its highest point in May.

4.2. UPC Barcelona University

From 2019 to 2020, UPC Barcelona conducted a similar analysis with similar results. Again, the disdrometer, which was used as a reference, recorded 347 precipitation events.

Metric	**RMA**	**IMERG**
Accuracy	0.71	0.67
Error Rate	0.29	0.23
Sensitivity (Recall)	0.46	0.49
Specificity	0.95	0.86
Precision	0.89	0.78
False Positive Rate (FPR)	0.05	0.14
F1-score	0.61	0.60
Matthews Correlation Coefficient (MCC)	0.46	0.37
Kappa	0.41	0.35

Table 6: RMA IMERG intercomparison metrics for Barcelona site

Table 6 shows that RMA exhibits slightly higher accuracy (71%) compared to IMERG (67%), indicating a better overall performance in correct classification. However, this comes with a trade-off in terms of sensitivity, where IMERG (49%) surpasses RMA (46%), making IMERG more effective

in correctly identifying positive cases. However, this increased sensitivity of IMERG leads to a higher False Positive Rate (FPR) of 14% compared to just 5% for RMA. This suggests that while IMERG is more sensitive, it is also more prone to false alarms, which could be a disadvantage in applications where false positives are critical. Specificity, which measures the ability to correctly identify negative cases, is markedly higher for RMA (95%) compared to IMERG (86%). This implies that the RMA is more reliable in avoiding false positives, complementing its lower FPR.

In terms of precision, RMA again outperforms IMERG, scoring 89% against 78%. This indicates that the predictions of positive cases by RMA are more often correct. The F1-score, a balance between precision and recall, is nearly identical for both methods, with RMA at 61% and IMERG at 60%. This suggests that despite their different strengths and weaknesses, the overall trade-off between precision and recall is balanced in both methods. The Matthews Correlation Coefficient (MCC), which takes into account the four confusion matrix categories, shows that the RMA has a higher value (46%) compared to IMERG (38%), indicating better overall performance in terms of predictive capabilities. Finally, the Kappa statistic, which measures the agreement between the methods, is also slightly higher for RMA (41%) than for IMERG (35%), indicating a stronger consistency in RMA's predictions compared to IMERG.

In conclusion, RMA offers better specificity, precision, and overall reliability in classifications, making it more suitable for scenarios where avoiding false positives is crucial. However, IMERG's strength lies in its higher sensitivity, making it more adept at detecting positive cases, albeit at the cost of increased false positives.

		RMA		
		No Rain	Rain	Total
Disdrometer	No Rain	328(94.50%)	19(5.50%)	347
	Rain	187(54%)	160(46%)	347
	Total	515	179	694

Table 7: Confusion Matrix Disdrometer - Rain Masking Algorithm

Table 7 shows that out of 347 instances, the RMA correctly identified 328 instances of no rain (94.5%) and 19 instances of rain (5.5%) when there was no rain. In contrast, during precipitation, the RMA correctly identified the

rain in 160 instances (46%) and missed it in 187 instances (54%). The total counts are 515 for no rain and 179 for rain, summing up to 694 instances overall.

		IMERG		
		No Rain	Rain	Total
Disdrometer	No Rain	298(86%)	49(14%)	347
	Rain	178(51%)	169(49%)	347
	Total	476	218	694

Table 8: Confusion Matrix Disdrometer - IMERG

Table 8 shows that IMERG, of the total instances, 86% of the non-rain events detected by the disdrometer were correctly classified by IMERG and 14% were misclassified as rain. For rain events, IMERG correctly identified 49% but misclassified 51% as not rain. Overall, IMERG demonstrates a good performance in detecting non-rain events, but its accuracy in detecting rain events is lower.

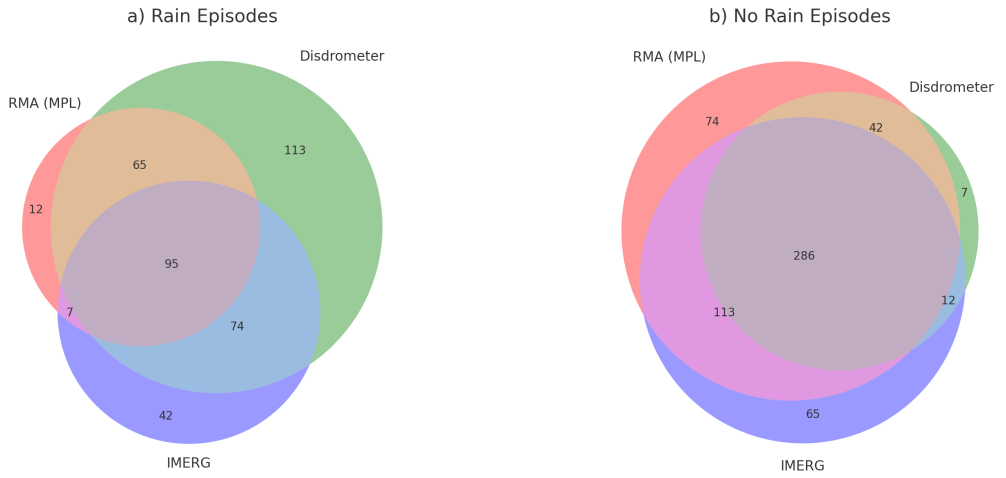

Figure 5: Venn diagrams showing the overlap in detection of rain and no-rain events among IMERG, RMA, and the Disdrometer at UPC Barcelona. The numbers indicate the detected cases shared between the instruments as well as those unique to each, highlighting the performance of IMERG and RMA compared to the disdrometer.

Similarly to the GSFC intercomparison, Figure 5 visually presents the performance of both RMA and IMERG. For rain events, the disdrometer

detected 113 unique instances that were not identified by the other methods. IMERG uniquely detected 42 episodes, and RMA (MPL) detected 12. There were 95 episodes in which all three instruments agreed, and partial overlaps between the disdrometer and IMERG (65) and between IMERG and RMA (7) suggest differences in detection sensitivity. In no-rain episodes, the agreement increased, with all three instruments detecting 286 common cases, while RMA and IMERG showed some distinct detections (74 and 65, respectively). The Disdrometer only identified 42 unique no-rain episodes.

We now analyze the results with respect to the intensity of the rain.

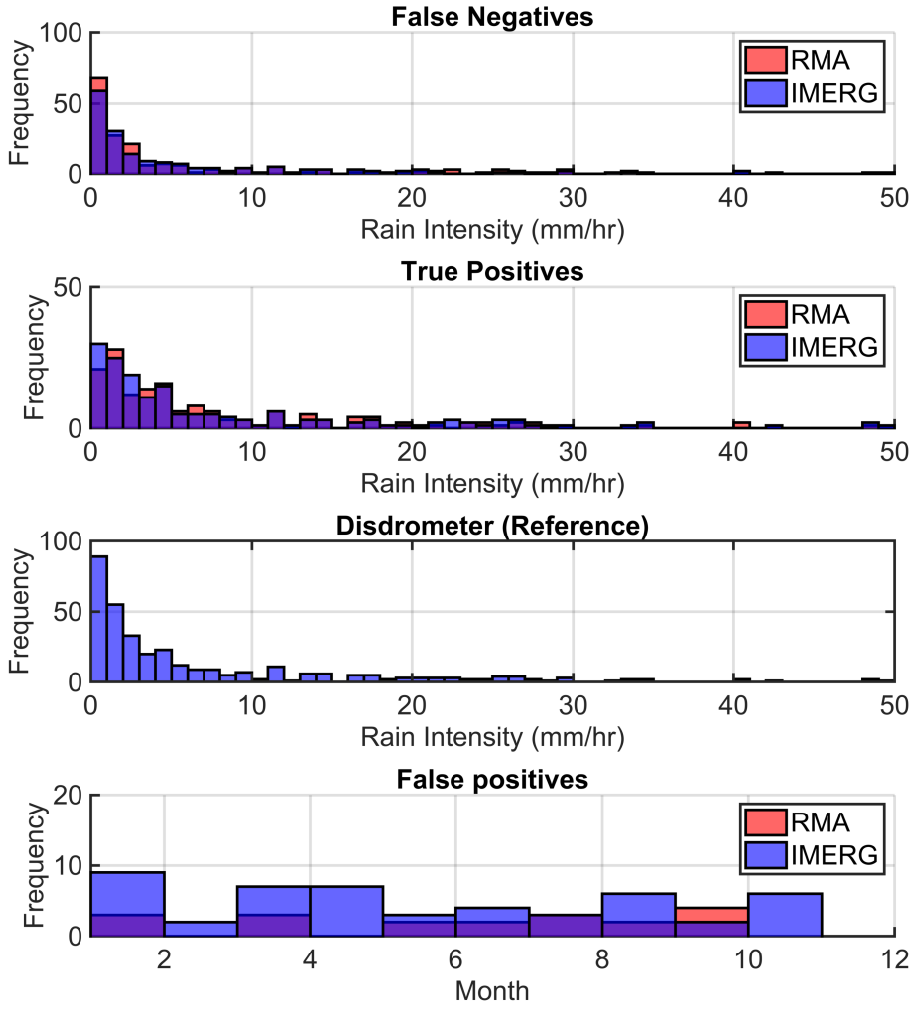

Figure 6: Above: Histogram of false negative events. Middle: Histogram of true positives. Lower: Histogram of false positives with respect to month. Frequency is expressed in absolute (%) values.

Figure 6 shows that in Barcelona the two algorithms exhibit minimal differences. Concerning false negatives, RMA misses slightly more precipitation events between 0 and 3 mm / hour compared to IMERG, but at higher in-

tensities their performance is almost the same. For true positive detection, RMA demonstrates better precision in the 1 to 3 mm/hr range, while precision is identical at other intensities. IMERG records more false positives throughout the year, except in September.

4.3. Deep Analysis of Performance Metrics: MCC and Cohen's Kappa

While accuracy, sensitivity, and specificity provide foundational metrics, additional metrics like the MCC and Kappa offer a more nuanced view of the RMA performance, particularly in the context of meteorology, where datasets are often imbalanced with more frequent no-rain than rain events. For instance, at GSFC site, the RMA achieved an MCC of 0.46 compared to IMERG's 0.37, indicating a stronger agreement between the RMA predictions and the observed data from the disdrometer when considering both correct and incorrect classifications. This metric is particularly useful because it balances the influence of all four components in the confusion matrix: true positives, true negatives, false positives, and false negatives, providing a robust measure that is not biased by class distribution. The higher MCC score for RMA suggests that it is better at distinguishing rain events from non-events in conditions of uneven event distribution, a common challenge in precipitation studies. Cohen's Kappa, another key metric, adjusts for the likelihood of random agreement, which is critical in meteorological algorithms where variability and event sparsity can introduce chance matches. At GSFC, RMA's Kappa was 0.41, notably higher than IMERG's 0.29, indicating that RMA's rain detection capability substantially exceeds what could happen by chance. Similarly, at UPC, RMA showed a Kappa of 0.41 versus IMERG's 0.35, further reinforcing the RMA's consistency across different geographic locations. Kappa's adjustment for random chance is particularly relevant for rare event detection, as it helps confirm that positive precipitation detections by the RMA are not merely coincidental but reflect true algorithmic performance. Thus, both the MCC and Kappa metrics provide additional confirmation of RMA reliability, validating that the sensitivity and specificity of the algorithm reflect true predictive power even under challenging and imbalanced conditions. These metrics highlight the robustness of the RMA in capturing significant rain events without being overly influenced by frequent instances of no rain, making it a valuable tool for accurate and reliable precipitation monitoring in global meteorological studies. A summary of the intercomparison at both locations can be found in Table 9.

Metric	GSFC		UPC	
	RMA	**IMERG**	**RMA**	**IMERG**
Accuracy	0.72	0.66	0.71	0.67
Error Rate	0.28	0.34	0.29	0.33
Sensitivity (Recall)	0.63	0.40	0.46	0.49
Specificity	0.81	0.91	0.95	0.86
Precision	0.78	0.83	0.89	0.78
False Positive Rate (FPR)	0.19	0.09	0.05	0.14
F1-Score	0.69	0.54	0.61	0.60
Matthews Correlation Coefficient (MCC)	0.46	0.37	0.46	0.38
Cohen's Kappa	0.41	0.29	0.41	0.35

Table 9: Summary of intercomparison at GSFC and UPC

5. Challenges in Intercomparison

In this section, we analyze particular instances where there are inconsistencies between the rain masking algorithm and the disdrometer, focusing on the antidiagonal entries of the confusion matrix presented in Figure 2. These scenarios, wherein one system registers precipitation while the other does not, are critical for comprehending the limitations and disparities intrinsic to precipitation detection methodologies. Furthermore, we note some of the challenges with ground-based lidar to satellite comparisons, particularly as they relate to our future EarthCARE validation.

5.1. False Negative: Low depolarization with low rain rate; 5 February 2020, GSFC

During this day, from 0500UTC to 0900UTC, the Rain Masking Algorithm (RMA) fails to detect rain reaching the surface, potentially due to the reduced volume depolarization ratio (VDR). Despite this, the algorithm reports several instances of virga, which is precipitation that evaporates before reaching the ground, during this time period. This phenomenon often occurs under conditions of strong evaporation. A detailed analysis of both the lidar signal and the VDR indicates that precipitation is not sufficient to significantly enhance the depolarization of the lidar signal beyond 0.06, which is the threshold required for detection by the RMA. This phenomenon may be attributed to either a scarcity of raindrops or particular microphysical characteristics of precipitation. Between approximately 0500 and 1000UTC

(Figure 7), the disdrometer identifies continuous precipitation, although the rain rate is considerably low (< 0.1 mm hr^{-1} on average). IMERG also detects rain at a higher rain rate during this time period, suggesting widespread rain that occurs throughout the region.

The NRB signal indicates that precipitation occurs periodically from 0500UTC to 0900UTC, as evidenced by the gray to white streaks below 3 km in the composite NRB plot, Figure 7a. During this interval, the VDR signal frequently remains below the 0.06 threshold, rendering the RMA incapable of detecting rainfall, while still identifying virga. In other instances where the RMA does not detect precipitation throughout the atmospheric column, we observe that the precipitation intensity recorded is negligible, with values not exceeding 0.001 mm hr^{-1}. This observation aligns with the algorithm's inability to identify significant precipitation events under such low-intensity conditions that translate into low depolarization.

Analyzing all undetected cases of RMA, we found that almost half are for precipitation events less than 2.5 mm hr^{-1}. We can speculate that, for these particular cases, the depolarization of the rain is below the threshold. Most undetected episodes are for precipitation with an intensity less than 0.025 mm hr^{-1}. It is possible to hypothesize that the concentration of raindrops is too low to cause the VDR signal to depolarize to a level that exceeds the necessary threshold. In the future, various thresholds will be tested to identify more precipitation events. Optimization should be done with the understanding that a too low threshold may misidentify aerosol layers as rain.

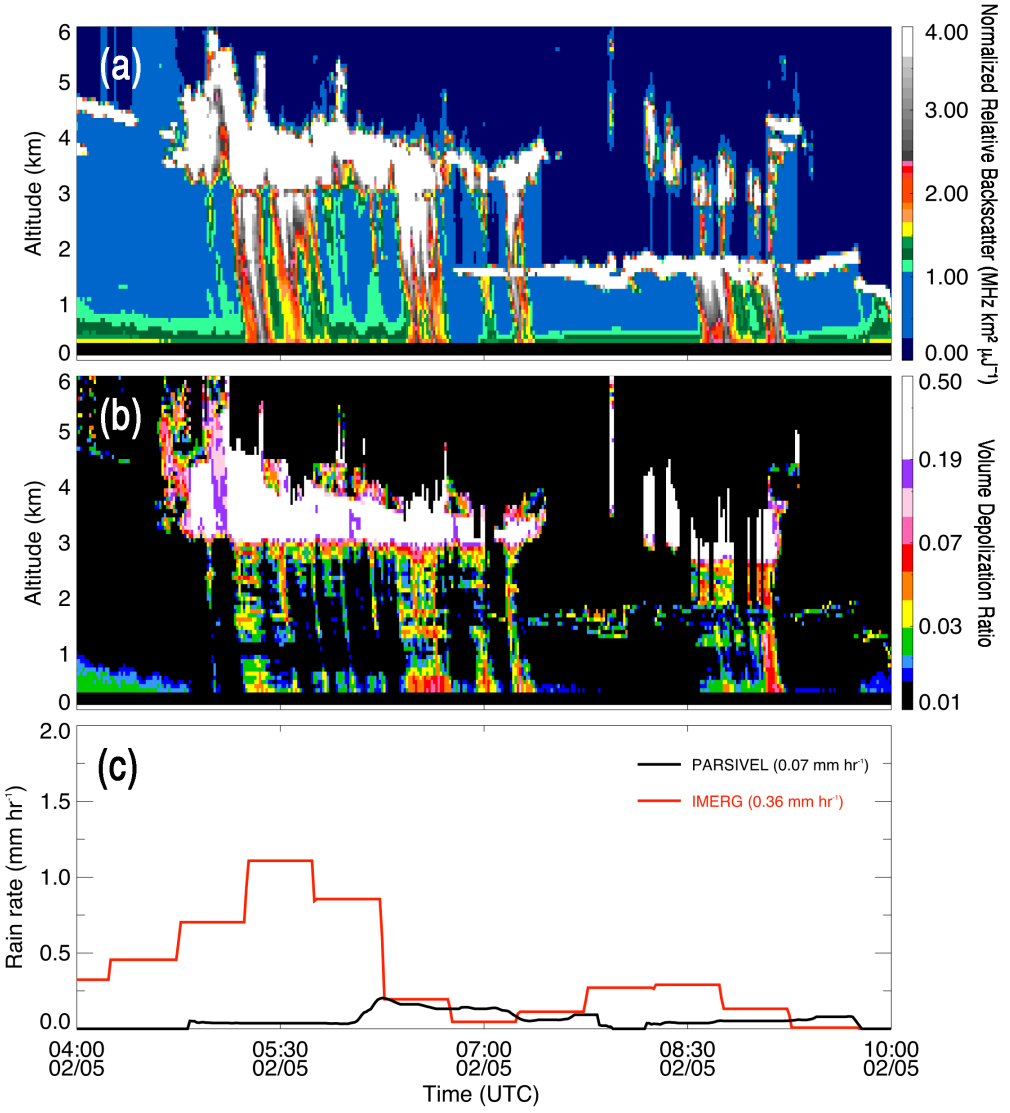

Figure 7: Tilted precipitation undetected by RMA from MPLNET lidar observation from 0400UTC to 1000UTC on 5 February 2020. Mean rain rates for Parsivel and IMERG (parentheses) and periods when RMA detects rain (gray shading) are given in (c). Note: VDR values with high uncertainty due to attenuation have been removed.

5.2. False Negative: Misclassified precipitation as cloud; 27 May 2021, GSFC

In this case, the disdrometer detects persistent rainfall from about 0100UTC to 0230UTC. However, rain detection from the RMA is more episodic. In part, this is explained by the RMA reporting virga from about 0145UTC to 0230UTC where the gray- to white streaks in the NRB plot and the pink- to purple streaks in the VDR plot (Figure 8 clearly do not extend to the surface. However, from about 0100UTC to 0130UTC, visual inspection of the data suggests that the rainfall should be continuous. The reason for the episodic nature of RMA retrieval is that cloud bases, which at this altitude are determined from gradients in the lidar signal, are being reported within the precipitation.

Because cloud detection is processed prior to precipitation detection, there is no way to retrieve precipitation once such misclassifications occur. In the future, it is planned to run the cloud and precipitation algorithms concurrently to reduce the frequency of these misclassifications. In this study, using a coarse one-hour temporal resolution resolution for validation, this specific case would record precipitation for both the disdrometer and the RMA. However, for higher temporal resolutions, cases like this could lead to a lower performance.

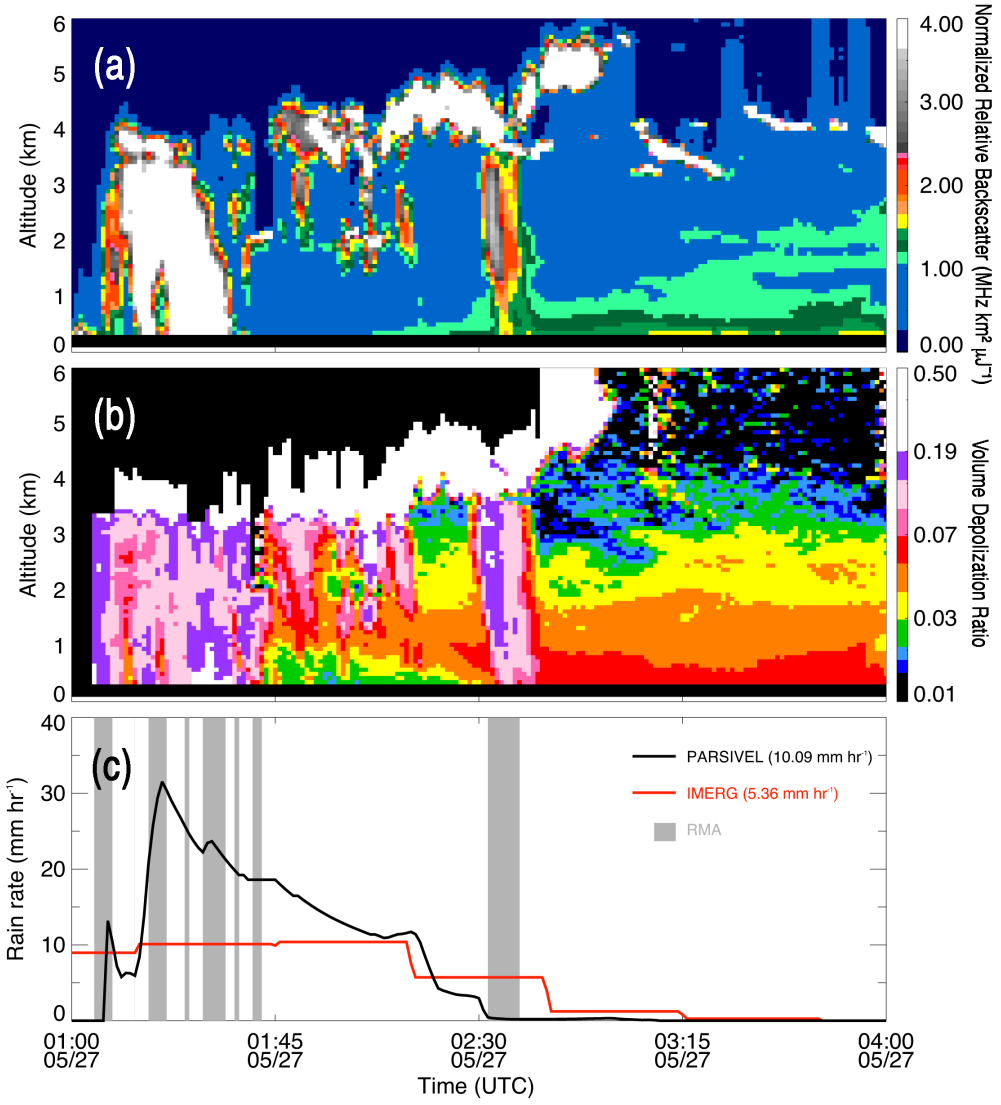

Figure 8: Episodic precipitation detection by the RMA due to cloud-rain misclassifications on 27 May 2021. Mean rain rates for Parsivel and IMERG (parentheses) and periods when RMA detects rain (gray shading) are given in (c). Note: VDR values with high uncertainty due to attenuation have been removed.

5.3. False Positive: Complex rain and dust scene; 8-9 July 2019, UPC Barcelona

Figure 9 shows a complex scene with a Saharan dust episode interacting with clouds at the UPC Barcelona site. The disdrometer, RMA, and IMERG correctly identify rain from about 0700UTC to 1800UTC. However, the RMA is less effective in distinguishing dust aerosols from rain within this scene. Visual inspection of the data after 1830UTC also suggests a higher likelihood of false positives due to dust-rain misclassifications. Currently, rain detection from the RMA at dusty sites must be given more scrutiny compared to other locations. Similarly to the situation with cloud-rain misclassifications, aerosol processing will be incorporated into future precipitation detection to reduce the frequency of false positives.

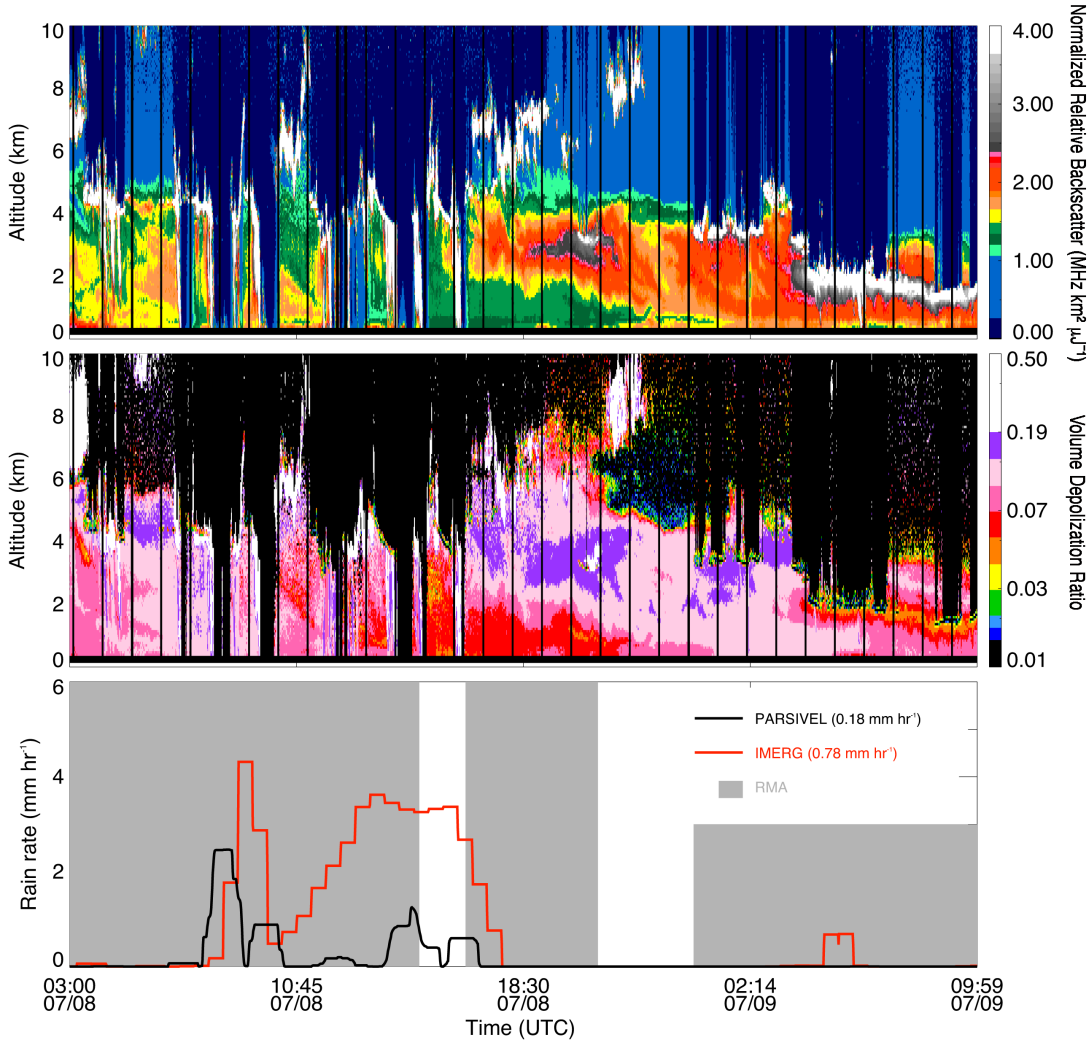

Figure 9: Dust aerosols potentially misclassified as precipitation at the UPC Barcelona site on 8-9 July 2019. Mean rain rates for Parsivel and IMERG (parentheses) and periods when RMA detects rain (gray shading) are given in (c). Note: VDR values with high uncertainty due to attenuation have been removed.

5.4. Other challenges

Beyond these algorithmic challenges, there are also limitations related to these comparisons of satellite retrievals from IMERG or EarthCARE and ground-based retrievals from MPLNET. The narrow field of view from the lidar represents a point source observation with a much smaller spatial ex-

tent than the wide swath of satellites. For example, IMERG retrievals are gridded to 0.1 by 0.1 degrees and averaged half-hourly, while the Cloud Profiling Radar (CPR) aboard EarthCARE has an instantaneous footprint of about 750 m. The C-TC and AC-TC Level 2 target classification products that will be used to determine the presence of precipitating clouds will have a maximum resolution of approximately 1 km [37]. This challenge of spatial matching is especially difficult with the localized nature of precipitation events. Ideally, a dense network of ground-based instruments, such as those used by [38], would be used to perform satellite validation. In the absence of such a dense network of lidars, it will be important to collect a large number of coincident EarthCARE overpasses to develop meaningful statistics.

6. Discussion and Conclusions

The Rain Mask Algorithm (RMA) implemented by NASA MPLNET demonstrates a strong performance in accurately detecting precipitation events, including virga, that is, a type of precipitation that does not reach the ground due to strong evaporation, which may be undetected by other instruments such as the disdrometer and IMERG. The algorithm achieves an overall accuracy of up to 72% in identifying rain events, compared to a co-located disdrometer taken as reference.

The intercomparison between RMA and co-located in situ disdrometers and the IMERG project provides valuable validation of the algorithm's performance. The results show high sensitivity and specificity, indicating the algorithm's ability to correctly detect both rain and no-rain events. The algorithm's precision is reasonably high, with a balanced F1 score indicating good accuracy in predicting positive rain events. The Matthews Correlation Coefficient and Kappa coefficient demonstrate moderate to good levels of correlation and agreement between the algorithm's detection and actual classifications.

In addition, we examine instances of detection errors. Certain types of precipitation fail to sufficiently depolarize the laser signal, resulting in their non-detection by the Rain Masking Algorithm, which requires a minimum Volume Depolarization Ratio of 0.06. This specific threshold is selected as a compromise to prevent aerosols from being misclassified as rain. In subsequent studies, the algorithm will incorporate the backscattered signal (NRB) alongside the VDR to accurately identify rainfall events. In other instances, the algorithm detected precipitation from artifacts due to heavy rains that

had previously occurred. In this situation, future research to optimize the algorithm will also take into account the scattered signal. More research and analysis are needed to determine the underlying factors that contribute to misdetected cases and refine the rain detection process.

The study's findings highlight the importance of accurate precipitation detection for various applications, including meteorology, hydrology, climate research, and disaster response. The rain mask algorithm, validated through intercomparison, provides a valuable tool to improve our understanding of global precipitation dynamics and advance the goals of the EarthCARE project.

In conclusion, the rain mask algorithm implemented in the NASA MPLNET product, in conjunction with the EarthCARE project, offers a promising approach to accurately detect precipitation. More research and analysis are needed to enhance the algorithms' capabilities and address potential sources of error, ultimately improving the accuracy of precipitation detection and our understanding of global precipitation dynamics in the context of the EarthCARE mission.

References

[1] D. Pimentel, J. Houser, E. Preiss, O. White, H. Fang, L. Mesnick, T. Barsky, S. Tariche, J. Schreck, S. Alpert, Water resources: Agriculture, the environment, and society, BioScience 47 (1997) 97–106. doi:10.2307/1313020.

[2] O. Cifdaloz, A. Regmi, J. M. Anderies, A. A. Rodriguez, Robustness, vulnerability, and adaptive capacity in small-scale social-ecological systems: The pumpa irrigation system in nepal, Ecology and Society 15 (2010). doi:10.5751/ES-03462-150339.

[3] D. Dudgeon, A. Arthington, M. Gessner, Z. Kawabata, D. Knowler, C. Lévêque, R. Naiman, A. Prieur-Richard, D. Soto, M. Stiassny, C. Sullivan, Freshwater biodiversity: importance, threats, status and conservation challenges, Biological Reviews 81 (2006). doi:10.1017/S1464793105006950.

[4] Y. Wu, T. Ming, R. de Richter, R. Höffer, H. Niemann, Large-scale freshwater generation from the humid air using the mod-

ified solar chimney, Renewable Energy 146 (2020) 1325–1336. doi:10.1016/J.RENENE.2019.07.061.

[5] H.-L. Yu, Y.-C. Lin, Analysis of space-time non-stationary patterns of rainfall-groundwater interactions by integrating empirical orthogonal function and cross wavelet transform methods, Journal of Hydrology 525 (2015) 585–597. doi:10.1016/J.JHYDROL.2015.03.057.

[6] S. Lolli, G. Vivone, J. R. Lewis, M. Sicard, E. J. Welton, J. R. Campbell, A. Comerón, L. P. D'Adderio, A. Tokay, A. Giunta, et al., Overview of the new version 3 NASA Micro-Pulse Lidar network (MPLNET) automatic precipitation detection algorithm, Remote Sensing 12 (1) (2019) 71.

[7] T. Wehr, Earthcare product validation requirements document: Level 1b/c and level 2a/b products, Tech. Rep. EOP-SM/3125/TW-tw, European Space Agency (June 2017).

[8] A. J. Illingworth, H. Barker, A. Beljaars, M. Ceccaldi, H. Chepfer, N. Clerbaux, J. Cole, J. Delanoë, C. Domenech, D. P. Donovan, et al., The EarthCARE satellite: The next step forward in global measurements of clouds, aerosols, precipitation, and radiation, Bulletin of the American Meteorological Society 96 (8) (2015) 1311–1332.

[9] T. Wehr, T. Kubota, G. Tzeremes, K. Wallace, H. Nakatsuka, Y. Ohno, R. Koopman, S. Rusli, M. Kikuchi, M. Eisinger, T. Tanaka, M. Taga, P. Deghaye, E. Tomita, D. Bernaerts, The earthcare mission – science and system overview, Atmos. Meas. Tech. 16 (2023) 3581–3608. doi:10.5194/amt-16-3581-2023.

[10] K. Mroz, B. P. Treserras, A. Battaglia, P. Kollias, A. Tatarevic, F. Tridon, Cloud and precipitation microphysical retrievals from the earthcare cloud profiling radar: the c-cld product, Atmos. Meas. Tech. 16 (2023) 2865—2888. doi:10.5194/amt-16-2865-2023.

[11] M. Löffler-Mang, J. Joss, An optical disdrometer for measuring size and velocity of hydrometeors, Journal of Atmospheric and Oceanic Technology 17 (2000) 130–139.

[12] A. Tokay, D. B. Wolff, W. A. Petersen, Evaluation of the new version of the laser-optical disdrometer, OTT Parsivel^2, Journal of Atmospheric and Oceanic Technology 31 (6) (2014) 1276–1288.

[13] C. Kidd, J. Tan, P.-E. Kirstetter, W. A. Petersen, Validation of the version 05 level 2 precipitation products from the GPM core observatory and constellation satellite sensors, Quarterly Journal of the Royal Meteorological Society 144 (2018) 313–328.

[14] G. Lempio, K. Bumke, A. Macke, Measurement of solid precipitation with an optical disdrometer, Advances in Geosciences 10 (2007) 91–97. doi:10.5194/ADGEO-10-91-2007.

[15] T. Raupach, A. Berne, Correction of raindrop size distributions measured by parsivel disdrometers, using a two-dimensional video disdrometer as a reference, Atmospheric Measurement Techniques 8 (2014) 343–365. doi:10.5194/AMT-8-343-2015.

[16] S. Lolli, L. P. D'Adderio, J. R. Campbell, M. Sicard, E. J. Welton, A. Binci, A. Rea, A. Tokay, A. Comerón, R. Barragan, J. M. Baldasano, S. Gonzalez, J. Bech, N. Afflitto, J. R. Lewis, F. Madonna, Vertically resolved precipitation intensity retrieved through a synergy between the ground-based NASA MPLNET lidar network measurements, surface disdrometer datasets and an analytical model solution, Remote Sensing 10 (7) (2018). doi:10.3390/rs10071102.

[17] M. Ciofini, A. Lapucci, S. Lolli, Diffractive optical components for high power laser beam sampling, Journal of Optics A: Pure and Applied Optics 5 (3) (2003) 186.

[18] S. Lolli, W. Y. Khor, M. Z. Matjafri, H. S. Lim, Monsoon season quantitative assessment of biomass burning clear-sky aerosol radiative effect at surface by ground-based lidar observations in pulau pinang, malaysia in 2014, Remote Sensing 11 (22) (2019) 2660.

[19] J. R. Campbell, S. Lolli, J. R. Lewis, Y. Gu, E. J. Welton, Daytime cirrus cloud top-of-the-atmosphere radiative forcing properties at a midlatitude site and their global consequences, Journal of Applied Meteorology and Climatology 55 (8) (2016) 1667–1679.

[20] J. R. Campbell, D. A. Peterson, J. W. Marquis, G. J. Fochesatto, M. A. Vaughan, S. A. Stewart, J. L. Tackett, S. Lolli, J. R. Lewis, M. I. Oyola, E. J. Welton, Unusually deep wintertime cirrus clouds observed over the alaskan subarctic, Bulletin of the American Meteorological Society 99 (1) (2018) 27–32. doi:10.1175/BAMS-D-17-0084.1.

[21] S. Lolli, J. R. Campbell, J. R. Lewis, Y. Gu, J. W. Marquis, B. N. Chew, S.-C. Liew, S. V. Salinas, E. J. Welton, Daytime top-of-the-atmosphere cirrus cloud radiative forcing properties at singapore, Journal of Applied Meteorology and Climatology 56 (5) (2017) 1249–1257.

[22] J. B. Abshire, H. Riris, G. R. Allan, C. J. Weaver, J. Mao, X. Sun, W. E. Hasselbrack, S. R. Kawa, S. Biraud, Pulsed airborne lidar measurements of atmospheric CO_2 column absorption, Tellus B: Chemical and Physical Meteorology 62 (5) (2010) 770–783.

[23] G. Ehret, P. Bousquet, C. Pierangelo, M. Alpers, B. Millet, J. B. Abshire, H. Bovensmann, J. P. Burrows, F. Chevallier, P. Ciais, et al., Merlin: A French-German space lidar mission dedicated to atmospheric methane, Remote Sensing 9 (10) (2017) 1052.

[24] E. J. Welton, J. R. Campbell, J. D. Spinhirne, V. S. Scott III, Global monitoring of clouds and aerosols using a network of micropulse lidar systems. in lidar remote sensing for industry and environment monitoring, Proc. of SPIE, International Society for Optics and Photonics 4153 (2001) 151–158.

[25] J. R. Lewis, J. R. Campbell, E. J. Welton, S. A. Stewart, P. C. Haftings, Overview of MPLNET version 3 cloud detection, Journal of Atmospheric and Oceanic Technology 33 (10) (2016) 2113–2134.

[26] J. Campbell, D. Hlavka, E. Welton, C. Flynn, D. Turner, J. Spinhirne, V. Scott, I. Hwang, Full-time, eye-safe cloud and aerosol lidar observation at atmospheric radiation measurement program sites: Instruments and data processing., Journal of Atmospheric and Oceanic Technology 19 (2002) 431–442.

[27] E. J. Welton, S. A. Stewart, J. R. Lewis, L. R. Belcher, J. R. Campbell, S. Lolli, Status of the nasa micro pulse lidar network (MPLNET): overview of the network and future plans, new version 3 data products,

and the polarized mpl, in: EPJ Web of Conferences, Vol. 176, EDP Sciences, 2018, p. 09003.

[28] G. Huffman, D. Bolvin, D. Braithwaite, K. Hsu, R. Joyce, C. Kidd, E. Nelkin, S. Sorooshian, E. Stocker, J. Tan, D. Wolff, P. Xie, Integrated multi-satellite retrievals for the global precipitation measurement (GPM) mission (IMERG), Satellite precipitation measurement: Volume 1 (2020) 343–353doi:10.1007/978-3-030-24568-9_19.

[29] A. Y. Hou, R. K. Kakar, S. Neeck, A. A. Azarbarzin, C. D. Kummerow, M. Kojima, R. Oki, K. Nakamura, T. Iguchi, The global precipitation measurement mission, Bulletin of the American Meteorological Society 95 (5) (2014) 701 – 722. doi:10.1175/BAMS-D-13-00164.1.

[30] S. Prakash, A. Mitra, D. S. Pai, A. Aghakouchak, From TRMM to GPM: How well can heavy rainfall be detected from space?, Advances in Water Resources 88 (2016) 1–7. doi:10.1016/J.ADVWATRES.2015.11.008.

[31] J. Su, H. Lü, Y. Zhu, Y. Cui, X. Wang, Evaluating the hydrological utility of latest imerg products over the upper huaihe river basin, china, Atmospheric Research 225 (2019) 17–29.

[32] J. Fang, W. Yang, Y. Luan, J. Du, A. Lin, L. Zhao, Evaluation of the TRMM 3B42 and GPM IMERG products for extreme precipitation analysis over china, Atmospheric research 223 (2019) 24–38.

[33] E. Peinó, J. Bech, M. Udina, Performance assessment of gpm imerg products at different time resolutions, climatic areas and topographic conditions in catalonia, Remote Sensing 14 (20) (2022). doi:10.3390/rs14205085.
URL `https://www.mdpi.com/2072-4292/14/20/5085`

[34] L. Bissonnette, G. Roy, F. Fabry, Range–height scans of lidar depolarization for characterizing properties and phase of clouds and precipitation, Journal of Atmospheric and Oceanic Technology 18 (2001) 1429–1446. doi:10.1175/1520-0426.

[35] S. Lolli, W. Y. Khor, M. M. Z. Matjafri, H. S. Lim, Monsoon season quantitative assessment of biomass burning clear-sky aerosol radiative effect at surface by ground-based lidar observations in

pulau pinang, malaysia in 2014, Remote Sensing 11 (22) (2019). doi:10.3390/rs11222660.
URL https://www.mdpi.com/2072-4292/11/22/2660

[36] H. E. Brooks, M. L. Flora, M. E. Baldwin, A rose by any other name: On basic scores from the 2 × 2 table and the plethora of names attached to them, Artificial Intelligence for the Earth Systems 3 (2) (2024) e230104. doi:10.1175/AIES-D-23-0104.1.

[37] A. Irbah, J. Delanoë, G.-J. van Zadelhoff, D. P. Donovan, P. Kollias, B. Puigdomènech Treserras, S. Mason, R. J. Hogan, A. Tatarevic, The classification of atmospheric hydrometeors and aerosols from the earthcare radar and lidar: the a-tc, c-tc and ac-tc products, Atmospheric Measurement Techniques 16 (11) (2023) 2795–2820. doi:10.5194/amt-16-2795-2023.
URL https://amt.copernicus.org/articles/16/2795/2023/

[38] J. Tan, W. A. Peterson, A. Tokay, A novel approach to identify sources of errors in IMERG for GPM ground validation, Journal of Hydrometeorology 17 (2016) 2477–2491.